

Highly active and extremely stable L₁0-PtCoMn ternary intermetallic nanocatalyst for oxygen reduction reaction

Shou-Guo Qin ^{a,b}, Jia Liu ^{b,c}, Zhen-Yu Chen ^{a,b}, Xi-hao Liu ^{b,d}, Huiyan Feng ^b, Yudan Feng ^b, Zhi-Qun Tian ^{b,c}, Panagiotis Tsiakaras ^{e,*}, Pei-Kang Shen ^{b,c, **}

^a School of Chemistry and Chemical Engineering, Guangxi University, Nanning 530004, PR China

^b Collaborative Innovation Center of Sustainable Energy Materials, Guangxi Key Laboratory of Electrochemical Energy Materials, Institute of Science and Technology for Carbon Peak & Neutrality, Guangxi University, Nanning 530004, PR China

^c School of Physics Science and Technology, Guangxi University, Nanning 530004 PR China

^d School of Resources, Environment and Materials, Guangxi University, PR China

^e Laboratory of Alternative Energy Conversion Systems, Department of Mechanical Engineering, University of Thessaly, 1 Sekeri Str., Pedion Areos, Volos 38334, Greece



ARTICLE INFO

Keywords:

Catalyst
Platinum metal
Oxygen reduction reaction
Full cell
Ordered intermetallic compound

ABSTRACT

Herein, we report a manganese-stabilized ternary intermetallic compound L₁0-PtCoMn as a highly active and extremely stable nanocatalyst for oxygen reduction reaction (ORR). In the half-cell test, the mass activity (MA) and specific activity (SA) of the optimal component L₁0-PtCo_{0.8}Mn_{0.2} are approximately 8.5 and 8.1 times higher than Pt/C, respectively, showing outstanding ORR catalytic activity. In PEMFC tests, the L₁0-PtCo_{0.8}Mn_{0.2} cathode exhibits an excellent MA (0.954 A/mg_{Pt} at 0.9 V_{iR-free}) and a superior durability (only ~8.6% loss in MA and ~5 mV voltage drop at 0.8 A cm⁻² after 30k ADT cycles), surpassing most of reported Pt-based ORR catalysts. Theoretical calculations reveal that incorporating Mn not only optimizes the adsorption energy (ΔE_{O^*}) of the intermediate O^{*} and thus enhance ORR activity, but also facilitates the formation of the order-structured L₁0-PtCoMn alloy and strengthens the interatomic interaction forces, leading to its superb durability. This work provides new highlights for developing highly ORR performing nanocatalysts for PEMFCs.

1. Introduction

Platinum-based alloy nanoparticles (Pt-NPs) are widely used for the oxygen reduction reaction (ORR) in proton exchange membrane fuel cells (PEMFCs). The sluggish ORR kinetics of the cathode and the poor stability of catalysts still hinder the extensive application of PEMFCs [1, 2]. The development of catalysts with high activity, high stability, and low cost has become the key to promoting the commercialization of fuel cells. Extensive experiments and theoretical calculations demonstrated that PtM-NPs can turn the electronic structure of Pt through the strain and ligand effect, resulting in the weakening of the binding of the oxygenated intermediates OH^{*} and O^{*}, thus significantly enhancing ORR catalysis [3]. L₁0-PtM intermetallic compounds (IMCs) with a strong 3d-5d interaction between the transition-metal and Pt atoms within the uniformly arranged ordered crystal structure, exhibited a further enhanced performance compared to PtM alloys, showing great

catalytic activity and stability for ORR, such as L₁0-PtCo [4,5], L₁0-PtFe [6], L₁0-PtNi [7], and so on. Unfortunately, in the practical application of PEMFCs, the dissolution of the transition metals M (M=Fe, Co, Ni, etc.) and corrosion of carbon supports inevitably occur under continuous potential variations and harsh acidic operating environments. This not only leads to the degradation of the intrinsic activity of catalysts, but also the dissolved metal cations destroy the PEM and reduce the performance of the fuel cells [8–10]. Hence, it is essential to suppress the dissolution of metals while maintaining their enhancing effect on ORR activity, in order to enable catalysts to have high activity, stable structure, and electrochemical durability in practical scale fuel cell applications of MEAs.

Previously, it has been reported that adding a third element to binary alloys can effectively hinder the dissolution trend of transition metals and even result in an optimized O^{*} adsorption energy, thus a better activity, such as W-doped Pt₂CuW_{0.25} [11], Ga-doped L₁0-Pt₂CuGa [12],

* Corresponding author.

** Corresponding author at: Collaborative Innovation Center of Sustainable Energy Materials, Guangxi Key Laboratory of Electrochemical Energy Materials, Institute of Science and Technology for Carbon Peak & Neutrality, Guangxi University, Nanning 530004, PR China.

E-mail addresses: tsiak@uth.gr (P. Tsiakaras), pkshen@gxu.edu.cn (P.-K. Shen).

Ti-stabilized $\text{Pt}_3\text{Co}_{0.6}\text{Ti}_{0.4}$ [13], etc. However, further improving the efficiency of ternary alloys and even multi-component IMC catalysts for the ORR is still challenging. On the one hand, according to the Hume-Rothery rules, thermodynamically stable alloys are affected by the atomic radius, crystal structure, electronegativity, and atomic valence of the combined metals. Moreover, the complexity of ternary alloys may lead to phase segregation and affect the stability of the catalyst structure [14,15]. On the other hand, the synthesis of intermetallic compounds usually needs synthesis at high temperatures to promote atom diffusion and alloying and achieve disorder-order phase transition. However, high temperature also intensifies the sintering of particles, resulting in larger particle size, reduced active area, and reduced electrocatalytic activity [16,17]. We noticed that the atomic radii and electronegativity of cobalt and manganese atoms are similar, and that $\text{L1}_0\text{-PtCo}$ and $\text{L1}_0\text{-PtMn}$ have the same crystal structure [18,19]. Compared to other Pt-M alloys, there is less attention paid to manganese, which may be due to the relatively negative redox potential of manganese (Mn^{2+}/Mn , -1.185 V) making it difficult to prepare. Meanwhile, according to the Material project database, $\text{L1}_0\text{-PtMn}$ has a relatively negative alloy formation energy, which may lead to better structural stability of the alloy [20,21].

Aspired from the above, in this work we report sub-6 nm ordered ternary intermetallic compound $\text{L1}_0\text{-PtCoMn}/\text{C}$ nanoparticles, derived using a facile impregnation method, as effective ORR catalysts for fuel cells, in which the introduction of Mn plays multiple roles in tailoring the properties of the catalyst. Firstly, the difficulties arising from sintering and atom diffusion during the thermal annealing of the ordered intermetallic compounds can be effectively overcome by the action of carbon shells and transition metal oxides. Moreover, the carbon shell and transition metal oxide do not need subsequent removal treatment. Secondly, by controlling the composition of manganese in the alloy, the ORR intrinsic activity of $\text{L1}_0\text{-PtCo}_x\text{Mn}_{1-x}$ and the oxygen adsorption energy calculated by density functional theory (DFT) showed a volcano-type plot trend, revealing a relationship between the catalytic activity and the alloy components. Thirdly, the durability of $\text{L1}_0\text{-PtCo}_{0.8}\text{Mn}_{0.2}$ is significantly boosted by the Mn addition, as revealed by both half-cell tests, MEA operation, and DFT analysis. As a result, the mass activity (MA) and specific activity (SA) of the $\text{L1}_0\text{-PtCo}_{0.8}\text{Mn}_{0.2}$ reaches $1.11 \text{ A}/\text{mg}_{\text{Pt}}$ and $2.74 \text{ mA}/\text{cm}^2$ respectively, while the MA loss was 28% after 30k cycles in the half-cell test. At the same time, the MA of $\text{L1}_0\text{-PtCo}_{0.8}\text{Mn}_{0.2}$ reaches $0.954 \text{ A}/\text{mg}_{\text{Pt}}$ at the beginning-of-life (BOL), additionally exhibiting an 8.6% loss at the end-of-life (EOL) after 30k cycles in the MEA testing, which is a rare small loss compared to other works. Through experiments and theoretical calculations, it was shown that $\text{L1}_0\text{-PtCo}_{0.8}\text{Mn}_{0.2}$ exhibits high activity and extremely stability, and can be used as an efficient catalyst for the ORR in a PEMFC.

2. Experimental section

2.1. Catalyst synthesis

2.1.1. Reagents

Chloroplatinic acid hexahydrate ($\text{H}_2\text{PtCl}_6 \cdot 6 \text{ H}_2\text{O}$), Cobalt Chloride (CoCl_3), Manganese chloride (MnCl_2), aniline ($\text{C}_6\text{H}_7\text{N}$), manganese (II) acetylacetone ($\text{Mn}(\text{acac})_2$, 97%), cobalt (III) acetylacetone ($\text{Co}(\text{acac})_3$, 97%), isopropanol, anhydrous ethanol, hydrochloric acid (~37.5%), sulfuric acid (95–98%), perchloric acid (70–72%), and Nafion (5%wt) were purchased from Aladdin. Pt/C catalyst was purchased from TANAKA (Pt:40.1 wt%). Ketjenblack ECP-600JD carbon was obtained from Lion Corporation, Japan. All chemicals were used without any subsequent processing.

2.1.2. Synthesis of the Pt-Aniline/ $\text{Co}(\text{acac})_3/\text{Mn}(\text{acac})_2/\text{C}$ powders

The platinum-aniline complex was prepared, according to previous reports [22,23]. We chose Ketjenblack ECP-600JD as the carbon support. Pt-aniline, $\text{Co}(\text{acac})_3$, and $\text{Mn}(\text{acac})_2$ were used as Pt, Co, and Mn

precursors. The uniform platinum-aniline/ $\text{Co}(\text{acac})_3/\text{Mn}(\text{acac})_2/\text{C}$ powders were obtained as follows: first, 60 mg of the Pt-aniline complex was dissolved in 80 ml of anhydrous ethanol in a glass sample bottle and mixed under ultrasound for 10 min. Then, the precursors were added to the mixture according to the set ratio (1:1:0, 1:0.8:0.2, 1:0.5:0.5, 1:0.2:0.8, 1:0:1, 3:0:1), and sonicated for 10 minutes. Then, 90 mg of Ketjenblack ECP-600JD carbon was added to the mixture and sonicated for 1 h, followed by stirring for 24 h. Second, the suspension was dried under ultrasonic assistance at 80°C for 1 h. Third, the collected purplish black powder was thoroughly ground in a mortar for further use. Other samples with different platinum loading have the same preparation process, except for controlling the metal loading amount.

2.1.3. Synthesis of carbon-supported A1-PtCoMn , $\text{L1}_0\text{-PtCoMn}$, and other samples

The L1_0 alloys were obtained by a thermal annealing process. First, the powder mixture was thermally annealed in a high purity nitrogen atmosphere. The reaction temperature slowly increased (rate $45^\circ\text{C}/\text{h}$) from 25 to 700°C and kept for 1 h, then cooled to room temperature. Second, the powder was further heated to 700°C in an H_2/Ar atmosphere (5% percent of H_2 in Ar) at a rate of $5^\circ\text{C}/\text{min}$ and kept for 4 h, and then cooled to room temperature.

The synthesized samples were further acid washed at 80°C for 12 h in 0.5 M H_2SO_4 solution. After the acid wash, the samples were rinsed 3–4 times with deionized water. Then, the collected samples were dried in vacuum to obtain the L1_0 Pt-based alloy NPs. For comparison, a sample subjected only to the first thermal annealing and the subsequent acid cleaning was synthesized and denoted as A1 Pt-based alloy NPs.

2.2. Electrochemical characterization

An electrochemical workstation equipped with a three-electrode system (Pine, USA) was used to study (evaluate) the electrochemical performance of the electrocatalysts. The cyclic voltammetry curves (CV), linear sweep voltammetry curves (LSV), CO-adsorption stripping curves (CO), and accelerated durability tests (ADT) were obtained by a rotating disc electrode (RDE). The effective area of the glassy carbon RDE was 0.196 cm^2 . A uniform catalyst slurry of 3 mg was dispersed in 1 ml of solvent (950 μl isopropanol, 40 μl H_2O , and 10 μl Nafion solution). Then, the catalyst slurry was evenly and smoothly distributed on the RDE (the catalyst loading on the electrode was $0.153 \text{ mg}/\text{cm}^2$). After the catalyst was completely dried on the electrode surface, a drop of ultrapure water was added to the electrode surface to wet the catalyst surface to prevent pollution and bubbles. For comparison, we used 3 mg of Pt/C catalyst to prepare 2 ml of a catalyst slurry and added 10 μl of it dropwise to the electrode surface.

The LSV measurements were recorded in an oxygen-saturated 0.1 M HClO_4 solution and corrected for the $i\text{R}$ solution resistance. The test potential range was between 0.05 and 1.1 V , and the rotating and scanning speed were 1600 rpm and $10 \text{ mV}/\text{s}$, respectively. The MA and kinetic current (j_k) were estimated by the LSV from the Koutecký–Levich (K-L) equation:

$$j_k = \frac{j_d \times j}{j_d - j} \quad (1)$$

$$MA \left(\text{A} \cdot \text{mg}_{\text{pt}}^{-1} \right) = \frac{j_k \quad (\text{mA})}{Pt_{\text{loading}} \quad (\mu\text{g})} \quad (2)$$

Here, j_k is the kinetic current; j_d is the limiting current; j is the apparent current; Pt_{loading} is the quantity of Pt on the RDE surface; A_g is the geometric area of the RDE. For CV, the scanning potential range was 0.05– 1.1 V in a solution saturated with nitrogen gas. During catalyst activation, the scanning speed was $100 \text{ mV}/\text{s}$; when testing the CV profile, the scanning speed was $50 \text{ mV}/\text{s}$. For CO-stripping, the initial potential was maintained at 0.05 V in a 0.1 M HClO_4 solution saturated with carbon monoxide, allowing the CO gas to adsorb on the surface of

the RDE for 15 min. Subsequently, high-purity N₂ was used to purify the remaining CO gas in the solution for 15 min. The CV curve of CO-stripping was measured at a scanning rate of 50 mV/s and a scanning potential range of 0.05–1.1 V. The ECSA (electrochemical active surface area) and SA were estimated using the following equations:

$$ECSA \quad (m^2 \cdot g_{pt}^{-1}) = \frac{Q_{area} \quad (A \cdot V)}{0.42(\mu C \cdot cm^{-2}) \times 0.05(V \cdot s^{-1}) \times Pt_{loading} \quad (mg_{pt})} \times 10^5 \quad (3)$$

$$SA \quad (mA \cdot cm_{pt}^{-2}) = \frac{j_k \quad (mA)}{ECS \quad (cm_{pt}^2)} \quad (4)$$

Here, Q_{area} is the adsorption capacity; 0.42 is the charge density required for the electrooxidation of adsorbed CO on a Pt monolayer (H_{ads}, 0.21); 0.05 is the scanning speed.

2.3. Preparation and testing of MEA

The anode was a commercial carbon supported platinum catalyst (Pt/C, 40.1% wt., TKK), while the cathode was the sample catalyst to be tested. Using an electrostatic sprayer, the catalyst was evenly sprayed onto the gas diffusion layer, the cathode/anode platinum loading was controlled at 0.12/0.2 mg/cm², the active area of the MEA is 5.29 cm². Then, the prepared catalytic layer and a Nafion 211 membrane (DuPont) were pressed using a hot press. The working conditions of the hot press were 135 °C, 5 kg/cm², and 5 min. Finally, the prepared membrane electrode assembly was installed in the fixture of the graphite bipolar plate with three channel serpentine flow field. This work adopted the 850e Fuel Cell Test System manufactured by Scribner Company United States.

H₂-O₂/Air (anode-cathode) gas flow was used to record the fuel cell polarization curves. According to the DOE standards, the cell temperature was set at 80 °C, 100% relative humidity, and 150 kPa pressure. During the fuel cell operation, the gas flow rates of the anode and cathode were 400/400 sccm (H₂-O₂) and 400/2000 sccm (H₂-Air), respectively. For the accelerated durability test (ADT), a square wave potential of 0.6 V for 3 s was applied, and then rapidly changed to 0.95 V for 3 s. The subsequent durability cycles were tested respectively, and then the corresponding tests were carried out. The accelerated durability test conditions were: 100% humidity, 80 °C, atmospheric pressure, and H₂/N₂ with an anode and cathode gas flow of 75/200 sccm.

2.4. DFT calculations

We used the Vienna Ab initio simulation package (VASP) and the Perdew-Burke-Ernzerhof (PBE) functionals to perform all DFT calculations under the generalized gradient approximation (GGA) [24]. The spin polarization effect was also considered. We choose the projection-enhanced wave (PAW) potential to describe the ion nucleus and the plane wave basis set with a kinetic energy cut-off of 450 eV to consider the valence electrons [25,26]. The DFT-D3 empirical correction method was used to describe the van der Waals interactions. Geometry optimizations were performed with a force convergency smaller than 0.05 eV/Å. The original bulk structures of the Pt_xCo_yMn_z alloy were optimized before the construction of the surfaces. In the Pt-Pt_xCo_yMn_z (111) surfaces were two layers of a Pt-doped atom on the Pt_xCo_yMn_z (111) alloy surface with the half atoms fixed in all calculations. Monkhorst-Pack k-points of 4×4×1 were applied for all the surface calculations for Pt-Pt_xCo_yMn_z (111). The O^{*} adsorption energy (ΔE_{O^{*}}), using the energy of 1/2 O₂ as a reference, is given by the following formula:

$$\Delta E_{O^*} = E_{total} - E_{slab} - E_{reference} \quad (5)$$

The formation energy (ΔE_{form}) of each atom of the ternary alloy

compound was calculated using the following equation [27]:

$$\Delta E_{form} = \frac{E_{total} - N_{Pt}E_{Pt} - N_{Co}E_{Co} - N_{Mn}E_{Mn}}{N_{Pt} + N_{Co} + N_{Mn}} \quad (6)$$

Here, E_{total} is the total energy at the alloy equilibrium; E_{Pt}, E_{Co}, E_{Mn} is the total energy of Pt, Co, and Mn in the solid state, respectively; N_{Pt}, N_{Co}, N_{Mn} is the number of Pt, Co, and Mn atoms contained in each unit cell, respectively. To compare the interactions between the atoms, the strength of the reaction bond is quantified using the following calculation formula [28]:

$$IpCOHP(\varepsilon_F) = \int^{\varepsilon_F} pCOHP(E)dE \quad (7)$$

Here, I is the integral below Fermi level.

3. Results and discussion

3.1. Synthesis and characterization of nanoparticle catalysts

Sub-6 nm ordered ternary intermetallic L1₀-PtCoMn NPs catalysts were prepared by a simple ultrasound-assisted impregnation and a thermal annealing reduction method. The preparation of platinum-anilines is referred to in previous works [22,23]. The synthesis process and formation mechanism of the catalysts are shown in Fig. 1a. In order to efficiently disperse the metal precursors during drying and prevent metal leaching caused by solvent evaporation, an ultrasonic-assisted drying strategy was adopted to obtain a black powder. As shown in Figure S1, the metal precursor was evenly impregnated on the surface of the carbon layer without leaching. As shown in Figures S2(a-d), the metal precursor is deposited and dispersed uniformly on the carbon layer. Through the slow annealing process in nitrogen atmosphere, the metal is reduced and finally forms an alloy (denoted as Al Pt based NP). Subsequently, the alloy underwent a second thermal annealing in hydrogen-argon (5%+95%) atmosphere to achieve disordered-ordered phase transition.

The X-ray diffraction (XRD) shows different diffraction peak patterns for Pt/C, A1-PtCo_{0.8}Mn_{0.2}, and L1₀-PtCo_{0.8}Mn_{0.2} in Figure S3a, indicating the difference in the crystal structure of the nanoparticles. The fcc crystals of Pt (PDF#65–2868) and Pt alloys have four typical diffraction peaks corresponding to the (111), (200), (220), and (311) facets, respectively. However, the diffraction peaks corresponding to the (220) and (311) facets of the A1-PtCo_{0.8}Mn_{0.2} Pt-based alloy NPs are very weak or even absent, indicating that they have microcrystalline structures with ultrafine particle sizes [29]. The XRD pattern of L1₀-PtCo_{0.8}Mn_{0.2} shows an ordered fcc structure with superlattice peaks of (001) and (110) facets at about 24 and 33.3 degrees, respectively. The diffraction peak of the (111) facet of L1₀-PtCo_{0.8}Mn_{0.2} is at 41.3 degrees, which is different from the diffraction peaks corresponding to the (111) crystal plane of Pt (at 39.8 degrees) and L1₀-PtCo (41.5 degrees, PDF#65–8969), because the Co and Mn atoms enter the lattice of Pt and cause crystal plane compression. Therefore, the crystal strain and ligand effect will affect the lattice parameters [30]. Figures S3(b and c) shows the FWHM (full width at half maxima) obtained by fitting the peaks of the XRD spectra, and then, using the Debye-Scherrer equation, the average crystallites sizes of L1₀-PtCo_{0.8}Mn_{0.2} and Pt/C were calculated to be 5.60 nm and 2.93 nm, respectively.

Further, the TEM images in Figures S4(a-f) show that after the first thermal annealing, the A1-Pt-based NPs were well dispersed, while having a uniform ultrafine size; the TEM image of Pt/C is presented for comparison. The TEM image and the inset in Fig. 1b show a histogram of the particle size distribution of A1-PtCo_{0.8}Mn_{0.2} NPs, indicating that the maximum frequency distribution of particles' size is 2.2 nm, which is smaller than Pt/C (2.63 nm). The TEM images in Figures S5(a-e) show that after the second thermal annealing, L1₀-PtCo_xMn_{1-x} (x=0/0.2/0.5/0.8/1) NPs were highly dispersed without agglomeration and sintering. More interestingly, we found that with the increase of cobalt content in

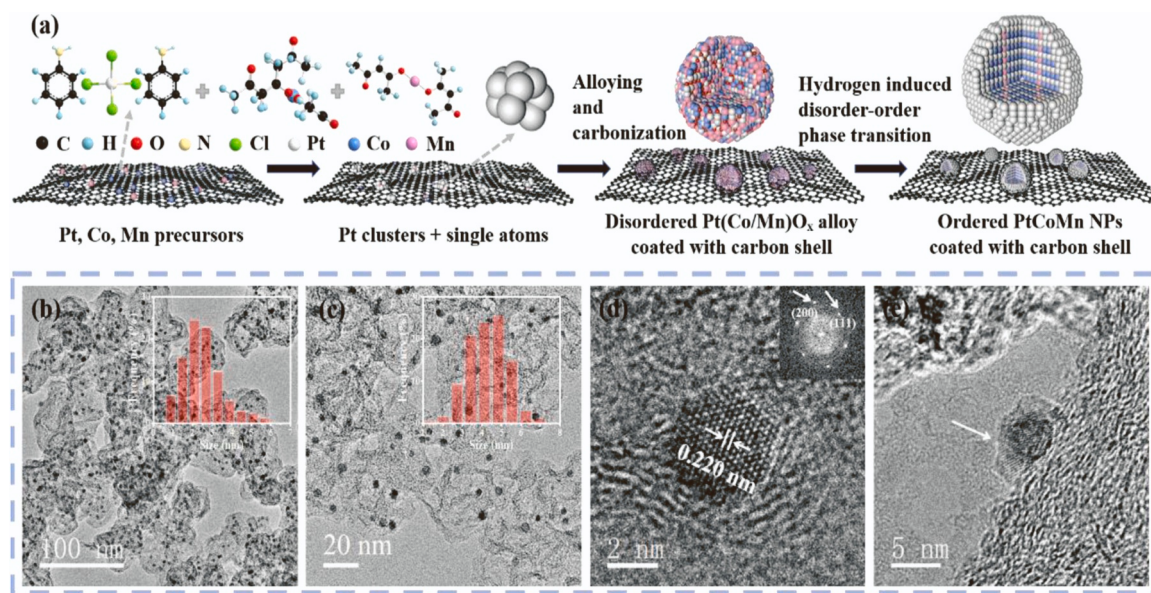


Fig. 1. Formation mechanism and characterization of Pt-Co-Mn NPs. (a) Schematic representation of the formation mechanism. (b) TEM image of ultrafine sized A1-PtCo_{0.8}Mn_{0.2} NPs. Inset: Size distribution histogram after the first thermal annealing. (c) TEM image of L₁₀-PtCo_{0.8}Mn_{0.2} NPs. Inset: Size distribution histogram after the second thermal annealing. (d) HR-TEM image of A1-PtCo_{0.8}Mn_{0.2} NPs before the second thermal annealing. Inset: the FFT image. (e) HR-TEM image of A1-PtCo_{0.8}Mn_{0.2} NPs coated with carbon shell.

L₁₀-PtCo_xMn_{1-x} ($x=0.2/0.5/0.8$) NPs, the particle size slightly increased (Table S1), indicating that manganese oxides have greater anti-sintering ability than cobalt oxides during thermal annealing. The TEM image in Fig. 1c shows a histogram of the particle size distribution, indicating that the maximum frequency distribution of particles' size is 4.95 nm, which is consistent with the XRD estimation of the average crystallites size and smaller than most reported ordered Pt-M NPs [4,23, 31].

To explore the reasons for the ultrafine size of nanoparticles, the anti-sintering mechanism of the catalyst synthesis was revealed. As shown in Figure S6a, we synthesized PtCo_{0.8}Mn_{0.2} NPs catalyst by changing different metal precursors. Obviously, although all samples have the same crystal structure, the average particle size of the particles can be calculated using the Scherrer's equation to be greater than 6 nm. Moreover, we can observe through TEM (Figures S6(b-f)) that there are significant differences in particle sizes among different synthesis schemes. More interestingly, we observed that when platinum-aniline and metal oxides were metal precursors, the particle size significantly decreased (Table S2). Therefore, we speculate that it may be due to the presence of metal oxides and carbon shells [22,23]. Further, the XRD patterns (Figure S7a) of A1-PtCo_xMn_{1-x} ($x=0/0.2/0.5/0.8/1$) nanoparticles show that as the cobalt component increases, the diffraction angle of the (111) facet of the fcc structure gradually increase, due to the smaller radius of the cobalt atom than that of the manganese atom, resulting in stronger strain effect. There is no diffraction peak of cobalt oxide in the XRD pattern, but the diffraction peak of manganese oxide can be seen in the XRD patterns of A1-PtMn and A1-PtCo_{0.2}Mn_{0.8}, while it does not appear in the alloys of the other components. Through the XPS spectra of PtCo_{0.8}Mn_{0.2} NPs, the existence of cobalt and manganese oxides and their changes during thermal annealing were discovered. After the first thermal annealing, typical peaks of cobalt oxide and manganese oxide can be seen from the XPS spectrum (Figure S7b), indicating the synthesis of alloys containing transition metal oxides. Obviously, as shown in Figure S7c, the peaks of transition metal oxides still exist after the second thermal annealing, indicating that transition metal oxides play a role in promoting diffusion and anti-sintering during the synthesis process [5,31].

In addition, the HR-TEM and FFT images of A1-PtCo_{0.8}Mn_{0.2} (Fig. 1d) show that the crystal facet spacing of the (111) surface of fcc is

0.220 nm, which is smaller than the crystal facet spacing of Pt (0.226 nm, PDF#65-2628) and larger than that of PtCo (0.216, PDF#65-8970), indicating the formation of alloy [32-34]. More interestingly, after the first thermal annealing, the small organic molecules of aniline and acetylacetone form carbon shells during the slow thermal annealing process, thereby preventing the sintering of NPs. The HR-TEM image of A1-PtCo_{0.8}Mn_{0.2} NPs (Fig. 1e) shows that the nanoparticles are coated with a carbon shell layer with a thickness of approximately 1 nm, which does not hinder the atomic diffusion and electron transfer in the catalyst [6,23].

As shown in Fig. 2a, the formation process of the sub-6 nm L₁₀-PtCo_{0.2}Mn_{0.8} alloy is explored through in-situ XRD, further revealing the anti-sintering effect of carbon shells. Clearly, at the initial stage of the reaction, with the rise of temperature, small organic molecules gradually evaporate and carbonize to form carbon shells. Subsequently, under the action of carbon shells, the metal is reduced and alloyed without obvious sintering. Moreover, the structural differences of L₁₀-PtCo_xMn_{1-x} ($x=0/0.2/0.5/0.8/1$) NPs were studied. The XRD patterns (Fig. 2b) show that after appropriate thermal annealing, multicomponent alloy NPs with superlattice diffraction peaks can be synthesized. However, the superlattice diffraction peaks of L₁₀-PtMn, L₁₀-PtCo_{0.2}Mn_{0.8} (green dotted line) and L₁₀-PtCo_{0.5}Mn_{0.5}, L₁₀-PtCo_{0.8}Mn_{0.2}, L₁₀-PtCo (blue dotted line) at about 33 degrees are slightly different, indicating the impact of the component engineering on the crystal structure. The enlarged sections (Fig. 2c) show that the diffraction angle in the XRD spectra gradually increases as the cobalt content in the component increases, indicating that the changes in the component lead to corresponding lattice compression. Therefore, the component engineering of the crystal can effectively adjust both the strain effect and electronic effect, and then affect ΔE_{O^*} for ORR, and improve the catalytic activity [2,35].

For L₁₀-PtCo [4,32] and L₁₀-PtFe [36], the magnetic hysteresis loops are commonly used to study their degree of order, but for multicomponent Pt-Co-Mn alloys, they can be used to qualitatively analyze the composition and magnetic behavior of the alloys. As shown in Fig. 2d, the A1-PtCo generally exhibits soft magnetic properties [19], while L₁₀-PtCo has a magnetic coercivity of 7.5 kOe, indicating that L₁₀-PtCo is a hard-magnet catalyst. For Pt-Mn alloy systems, the A1 phase is usually paramagnetic, but after the high-temperature annealing, it transforms into a chemically ordered L₁₀-PtMn structure with

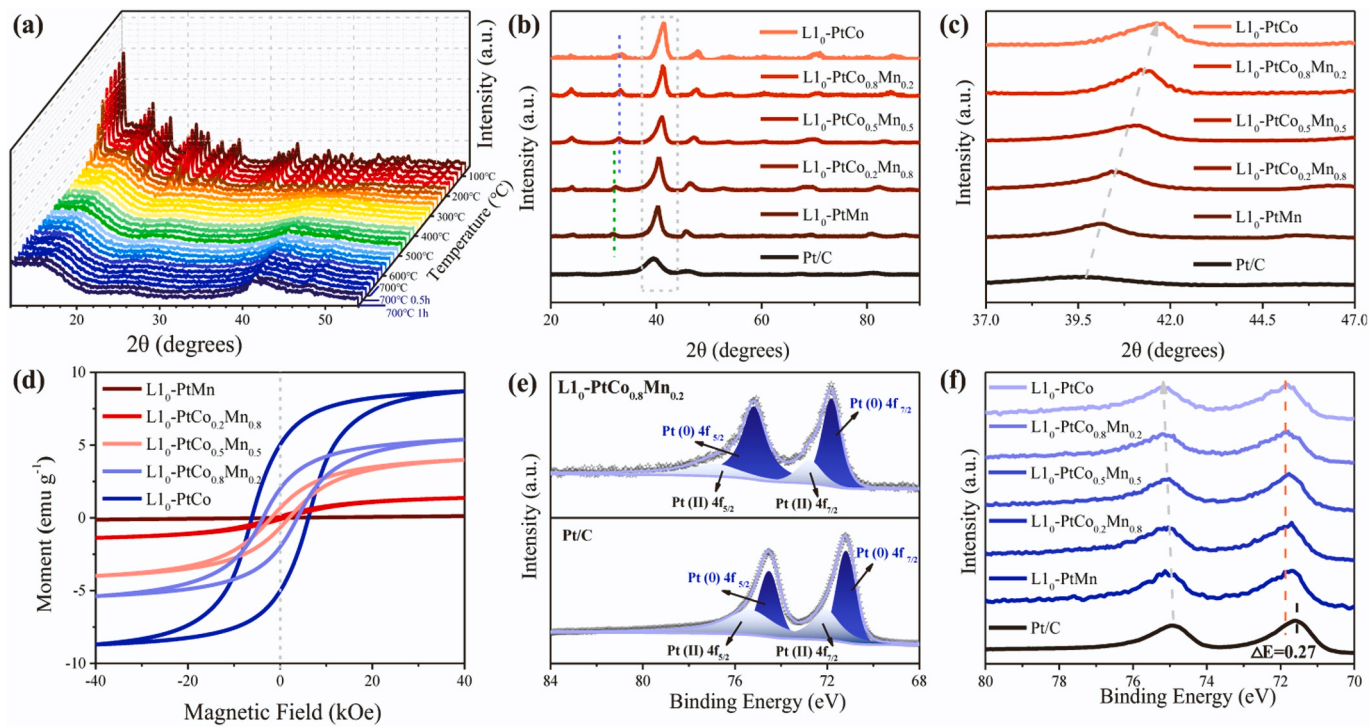


Fig. 2. Structural characterization and component engineering of $\text{PtCo}_x\text{Mn}_{1-x}$ NPs; (a) In-situ XRD patterns of Pt-Co-Mn NPs during the first thermal annealing process in terms of temperature and time-evolution; (b and c) the XRD patterns of $\text{L1}_0\text{-PtCo}_x\text{Mn}_{1-x}$ ($x=0/0.2/0.5/0.8/1$) NPs and commercial Pt/C. The enlarged section shows the change of lattice compression; (d) Magnetic hysteresis loops of $\text{L1}_0\text{-PtCo}_x\text{Mn}_{1-x}$ ($x=0/0.2/0.5/0.8/1$) NPs; (e) XPS spectra peak fitting for $\text{L1}_0\text{-PtCo}_{0.8}\text{Mn}_{0.2}$ NPs and Pt/C; (f) XPS spectra for $\text{L1}_0\text{-PtCo}_x\text{Mn}_{1-x}$ ($x=0/0.2/0.5/0.8/1$) NPs and Pt/C.

antiferromagnetic behavior, resulting in a magnetic induction intensity close to zero and a horizontal hysteresis loop [18,37]. Therefore, with the increase of the Co/Mn atomic ratio in the component, the behavior of chemically ordered fcc alloy NPs changes from anti-ferromagnetism to para-magnetism, and finally to hard magnetism, indicating that the composition engineering of the crystal can affect the magnetic behavior of the catalyst, and then affect the catalytic activity and stability of ORR [38–40].

XPS was applied to analyze the Pt chemical states in $\text{L1}_0\text{-PtCo}_{0.8}\text{Mn}_{0.2}$ NPs and further reveal the effect of component engineering on the electronic binding energy of Pt-based alloys. As shown in Fig. 2e, XPS spectrum of $\text{L1}_0\text{-PtCo}_{0.8}\text{Mn}_{0.2}$ shows that the binding energy moves towards a larger value relative to Pt/C, which indicates that there is a strong interaction between Pt atoms and Co/Mn atoms in the $\text{L1}_0\text{-PtCo}_{0.8}\text{Mn}_{0.2}$ structure (thus, electron transfer from Co/Mn to Pt), which also causes the d-band center to move down, which promotes the improvement of the catalytic activity through the weakening of the binding energy of the ORR intermediates [41]. Through the peak fitting analysis of XPS spectrum, it is found that Pt(0) in the metallic state accounts for a large proportion in $\text{L1}_0\text{-PtCo}_{0.8}\text{Mn}_{0.2}$ NPs, while platinum oxidized state is present at a lower fraction, which is conducive to the combination of O and OH, thereby improving the catalytic activity of ORR [42,43]. As shown in Fig. 2f, the XPS spectrum of Pt (4 f) clearly shows that, for Pt/C, there are two different photoelectron peaks at 71.5 eV and 74.85 eV; the shifted position of the corresponding photoelectron peaks in $\text{L1}_0\text{-PtMn}$ (71.55 eV and 74.89 eV) and $\text{L1}_0\text{-PtCo}$ (71.77 eV and 75.10 eV) indicate a good binding of Co and Mn atoms with Pt atoms. Therefore, Co atoms in $\text{L1}_0\text{-PtCoMn}$ alloy can significantly regulate the strain and ligand effects, while Mn atoms mainly play the role of anti-sintering and stabilizing the alloy. Specifically, as the Co/Mn atomic ratio in the component increases, the two photoelectron peaks of Pt (4 f) shift to higher values, which is due to the chemical shift caused by the different chemical binding states of Pt atoms in the different alloy components, indicating that the ligand effect is stronger

with the increase of cobalt content.

We used atomic resolution HAADF-STEM to analyze the structure and elemental composition of the $\text{L1}_0\text{-PtCo}_{0.8}\text{Mn}_{0.2}$ nanoparticles with two atomic-layer Pt shells. As seen from Fig. 3(a & b), the HAADF-STEM images show that the ordered $\text{L1}_0\text{-PtCo}_{0.8}\text{Mn}_{0.2}$ (CuAu-type, space group P4/mmm) core-shell structure is composed of platinum and cobalt/manganese atoms arranged alternately in light and dark, as well as platinum shells with 2–3 at. layers. In the second thermal annealing, the induction of hydrogen is beneficial to the alloying and the formation of platinum skin layer, and promotes the disordered-ordered transformation of the alloy to form ordered intermetallic compounds with core-shell structure [5,29].

For comparison, the HAADF-STEM images of $\text{A1-PtCo}_{0.8}\text{Mn}_{0.2}$ with an fcc structure and Pt_3Co with a L1_2 (Cu₃Au-type, space group Pm–3 m) structure are shown in Figures S8(a and b). It was found that the crystal shape of the alloy also changed due to the atomic rearrangement of the alloy.

The FFT patterns (Fig. 3c, Figures S8(c & d)) show that the L1_2 and L1_0 structures have distinct superlattice crystal facets of (100) and (001), respectively. Through measurement, the (001) and (110) crystal plane spacings of $\text{L1}_0\text{-PtCo}_{0.8}\text{Mn}_{0.2}$ are 0.368 nm and 0.27 nm, respectively. The outermost atomic arrangement of $\text{L1}_0\text{-PtCo}_{0.8}\text{Mn}_{0.2}$ was measured by alternating the intensity distribution (Figures S9a and S9b), further confirming the ordered structure of NPs. EDS line-profile of $\text{L1}_0\text{-PtCo}_{0.8}\text{Mn}_{0.2}$ NPs (Fig. 3d) shows that the energy of the outermost Pt atoms is significantly greater than that of the interior, while the outermost energy of the Co and Mn atoms is smaller than the internal energy, confirming the core-shell structure. As seen from the EDS elemental mappings (Fig. 3(e-h)) Pt and Co/Mn atoms are uniformly well-distributed in the NP, and the elemental composition is substantially consistent with the line profile. ICP-MS measurements (Table S3) show that the $\text{L1}_0\text{-PtCo}_{0.8}\text{Mn}_{0.2}$ NPs have a platinum loading of 15.96 wt% with a Pt:Co:Mn atomic ratio of nearly 1:0.82:0.23.

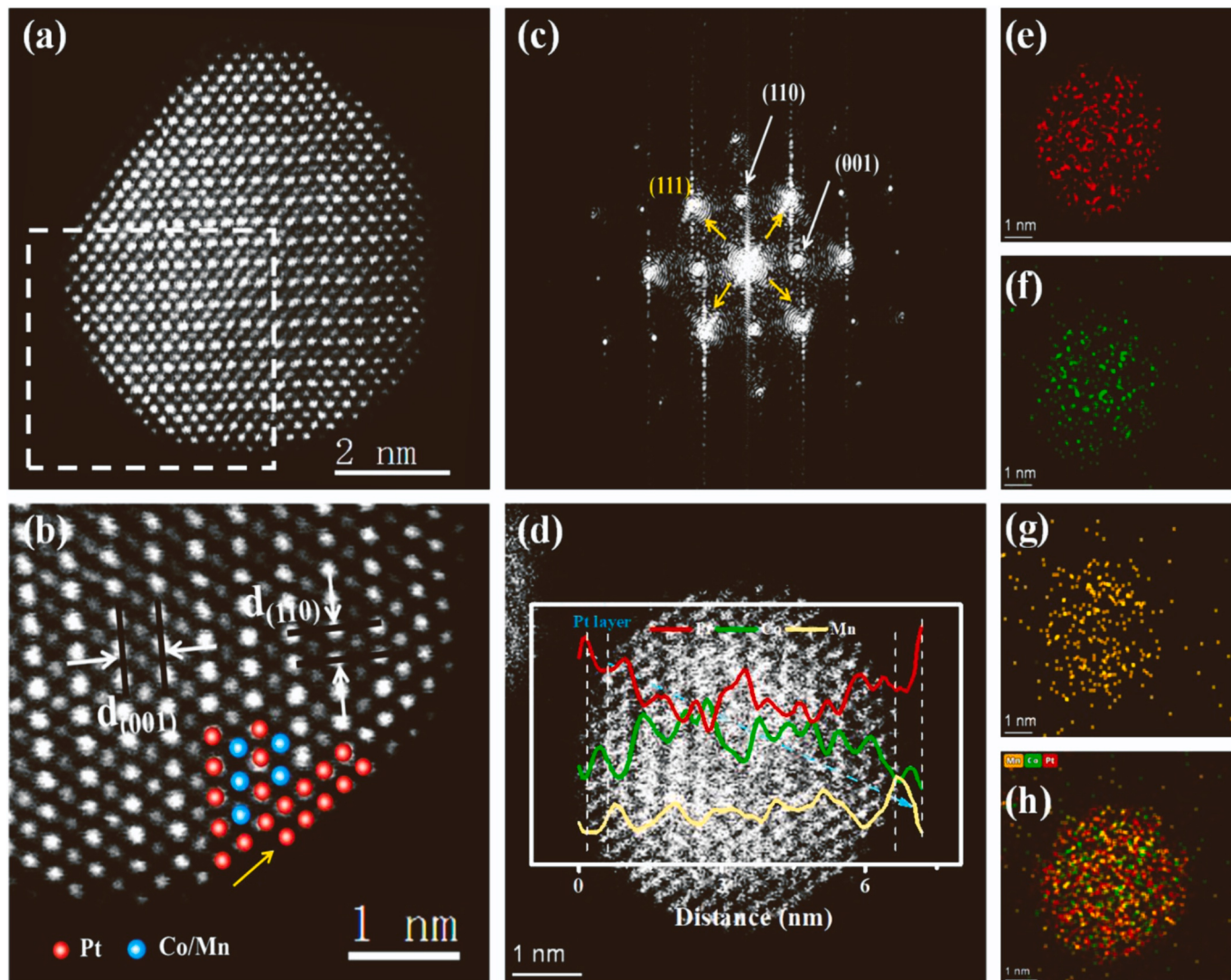


Fig. 3. Structure and elemental analysis of $\text{L1}_0\text{-PtCo}_{0.8}\text{Mn}_{0.2}$ NPs with a Pt shell by atomic-resolution HAADF-STEM; (a and b) HAADF-STEM image of $\text{L1}_0\text{-PtCo}_{0.8}\text{Mn}_{0.2}$ NPs. The enlarged section shows the core-shell structure; (c) FFT pattern of $\text{L1}_0\text{-PtCo}_{0.8}\text{Mn}_{0.2}$; (d) EDS line-profile of $\text{L1}_0\text{-PtCo}_{0.8}\text{Mn}_{0.2}$ NPs; (e-h) EDS elemental mappings of $\text{L1}_0\text{-PtCo}_{0.8}\text{Mn}_{0.2}$ NPs.

3.2. Catalyst activity for ORR

The LSV (Fig. 4a) shows that the $\text{A1-PtCo}_{0.8}\text{Mn}_{0.2}$ and $\text{L1}_0\text{-PtCo}_{0.8}\text{Mn}_{0.2}$ catalysts exhibit higher ORR activity compared to commercial Pt/C, with half-wave potentials ($E_{1/2}$) of 0.8824 V and 0.940 V vs. RHE, respectively, indicating that alloying and ordering can effectively improve the reaction activity. The schematic diagram (Fig. 4a inset) shows that the ORR kinetic energy barrier is overcome by achieving a phase transition from a disordered to an ordered structure, resulting in improved catalytic performance. It was found that $\text{L1}_0\text{-PtCo}_{0.8}\text{Mn}_{0.2}$ (Fig. 4c) shows the best catalytic activity compared to the other catalysts with different Co/Mn ratio.

As shown in the CV and CO curves (Figures S10(a and b)), the electrochemical surface areas (ECSA) of $\text{A1-PtCo}_{0.8}\text{Mn}_{0.2}$ and $\text{L1}_0\text{-PtCo}_{0.8}\text{Mn}_{0.2}$ are 78.1 and $40.5 \text{ m}^2/\text{g}_{\text{Pt}}$ (Table S4), respectively, which is the result of the combined action of ultra-small catalyst particle size and highly active crystal facet [44]. To analyze the effect of the components on the catalytic specific activity, the corresponding CV and CO curves were taken (Fig. 4b and Figure S10c), indicating that the ECSA of $\text{L1}_0\text{-PtCo}_x\text{Mn}_{1-x}$ ($x=0.2/0.5/0.8$) gradually increases with the increase in the manganese content of the component (Table S4), and confirms the conclusion of the anti-sintering mechanism induced by the Mn oxides.

However, the ECSA of $\text{L1}_0\text{-PtMn}$ is slightly different because the disordered-ordered phase transition process requires a higher annealing temperature or longer holding time in the absence of Co, resulting in the sintering of nanoparticles.

As shown in Fig. 4d, the Tafel plots of the kinetic current densities (j_{k}) show that the ordering and component engineering of the L1_0 alloys can effectively regulate the kinetics of the catalytic reactions and enhance ORR activity through the corresponding adjustment of the strain and ligand effect. Fig. 4(e and f) show the MA and SA of $\text{L1}_0\text{-PtCo}_{0.8}\text{Mn}_{0.2}$ with the values of $1.11 \text{ A}/\text{mg}_{\text{Pt}}$ and $2.73 \text{ mA}/\text{cm}^2$, indicating a high Pt utilization and intrinsic activity. Compared with Pt/C catalyst, MA and SA are increased by ~ 8.5 and ~ 8.1 times ($0.13 \text{ A}/\text{mg}_{\text{Pt}}$ and $0.34 \text{ mA}/\text{cm}^2$), respectively. The influence of the component ratio in $\text{L1}_0\text{-PtCo}_x\text{Mn}_{1-x}$ ($x=0/0.2/0.5/0.8$) catalysts can also be clearly seen in Table S4, indicating that component engineering is a practicable method to enhance the intrinsic activity of catalysts. Among the $\text{L1}_0\text{-PtCo-Mn}$ NPs, $\text{L1}_0\text{-PtCo}_{0.8}\text{Mn}_{0.2}$ exhibits the best catalytic activity, indicating that this component has suitable oxygen adsorption energy in ORR, which leads to the increase of reaction activity.

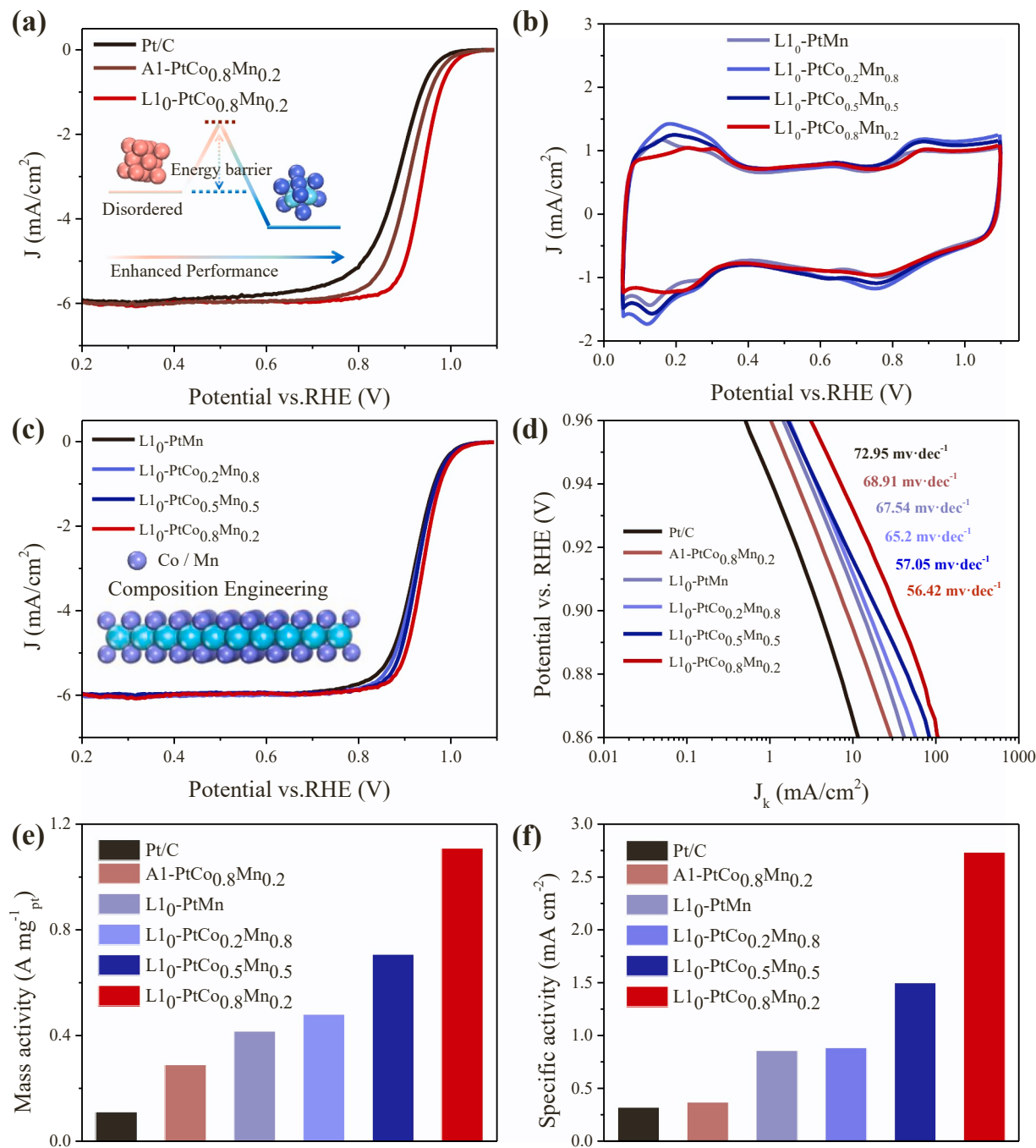


Fig. 4. Performance of electrocatalysts for ORR. (a) LSV curves of Pt/C, A1-PtCo_{0.8}Mn_{0.2}, and L1₀-PtCo_{0.8}Mn_{0.2}; (b) CV curves of L1₀-PtMn and L1₀-PtCo_xMn_{1-x} (x=0.2/0.5/0.8); (c) LSV curves of L1₀-PtMn and L1₀-PtCo_xMn_{1-x} (x=0.2/0.5/0.8). Inset: Schematic illustration showing the effect of component engineering on catalyst performance; (d) Tafel plots of Pt/C, A1-PtCo_{0.8}Mn_{0.2}, and L1₀-PtCo_xMn_{1-x} (x=0/0.2/0.5/0.8) NPs, in which j_k is the kinetic current density; (e) MA at 0.9 V; (f) SA at 0.9 V.

3.3. Durability of catalyst for ORR

The LSV and CV curves (Fig. 5(a and d)) show that the $E_{1/2}$ loss of L1₀-PtCo_{0.8}Mn_{0.2} after 30k ADT cycles is only 15.1 mV, while the loss of Pt/C catalyst after 30k ADT cycles is 45 mV, indicating that the catalyst has excellent durability. We also note that the CO stripping curve profiles are (Figure S11) consistent with LSV and CV, indicating that there is no obvious change in the composition and morphology of the catalyst surface after 30k ADT cycles [45,46]. By normalizing the ORR LSVs using the K-L equation (Fig. 5(h and i)), it was found that L1₀-PtCo_{0.8}Mn_{0.2} exhibits only 28% loss in MA and 26.7% loss in SA

after 30k ADT cycles (Pt/C lost 49%/32% in MA/SA after 30k cycles). The LSV and CV curves for different ADT cycles (Fig. 5g) show that after 10k cycles, the area of the hydrogen adsorption zone first increases and then decreases, while the area of the oxygen zone sequentially reduces, indicating that there is no significant agglomeration of NPs. The TEM images shown in Figure S12(a-e) also confirm the abnormal stability of the catalysts during ADT, where L1₀-PtCo_xMn_{1-x} (x=0.2/0.5/0.8/1) NPs exhibit uniform size and dispersion, while there is no obvious NPs aggregation on the carbon support from BOL to EOL.

The effect of component engineering on the stability of L1₀ alloy NPs was deeply investigated in accelerated durability tests. As illustrated in Fig. 5

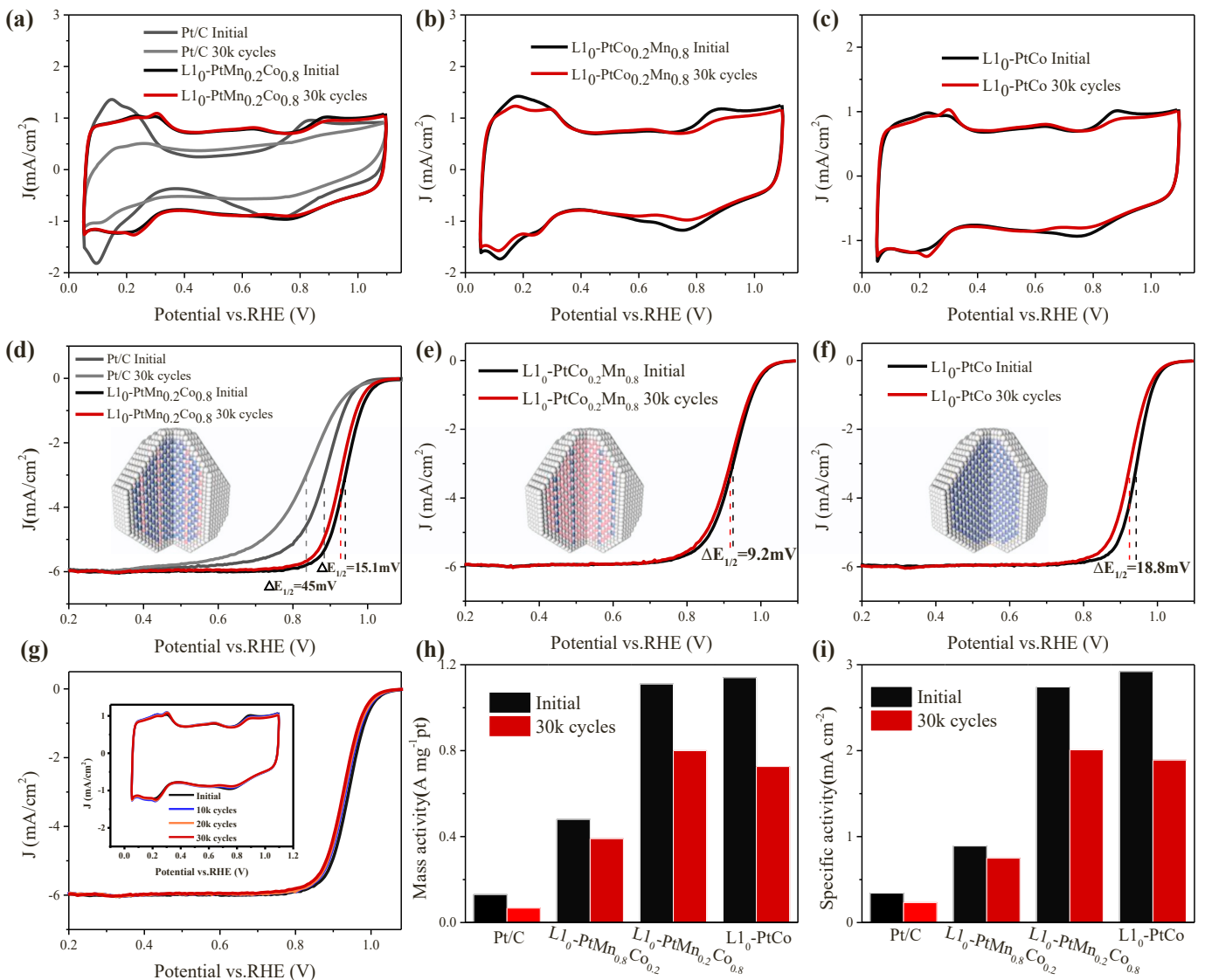


Fig. 5. Durability of electrocatalysts for ORR. (a-c) CV curves of the $\text{L1}_0\text{-PtCo}_{0.8}\text{Mn}_{0.2}$, $\text{L1}_0\text{-PtCo}_{0.2}\text{Mn}_{0.8}$, and $\text{L1}_0\text{-PtCo}$ catalysts, respectively. (d-f) LSV curves of the $\text{L1}_0\text{-PtCo}_{0.8}\text{Mn}_{0.2}$, $\text{L1}_0\text{-PtCo}_{0.2}\text{Mn}_{0.8}$, and $\text{L1}_0\text{-PtCo}$ catalysts, respectively. Inset (d, e, and f): Schematic illustration showing the model of the atomic arrangement of the $\text{L1}_0\text{-PtCo}_{0.8}\text{Mn}_{0.2}$, $\text{L1}_0\text{-PtCo}_{0.2}\text{Mn}_{0.8}$, and $\text{L1}_0\text{-PtCo}$ catalysts, respectively; (g) LSV curves of the $\text{L1}_0\text{-PtCo}_{0.8}\text{Mn}_{0.2}$ catalyst after various numbers of ADT cycles. Inset: Corresponding CV curves; (h) MA at 0.9 V; (i) SA at 0.9 V.

(b & e), after a 30k ADT cycles, $\text{L1}_0\text{-PtCo}_{0.2}\text{Mn}_{0.8}$ shows a negative shift of only ~ 9.2 mV in $E_{1/2}$.

Notably, the MA and SA of the $\text{L1}_0\text{-PtCo}_{0.2}\text{Mn}_{0.8}$ catalyst display a drop of 18.6% and 15.3%, respectively (Table S5). Comparatively, the $\text{L1}_0\text{-PtCo}$ (Fig. 5(c & f)) exhibits a negative shift by ca. 18.8 mV $E_{1/2}$ and an apparent loss of 36.7% in MA and 35.4% in SA. This indicates that the introduction of Mn metal atoms into L1_0 alloy can significantly enhance the stability of the catalyst in the oxygen reduction reactions, and consistent conclusions were deduced for $\text{L1}_0\text{-PtMn}$, $\text{L1}_0\text{-PtCo}_{0.5}\text{Mn}_{0.5}$ and $\text{L1}_2\text{-Pt}_{3}\text{Co}$ (Figure S13). For $\text{L1}_0\text{-PtCoMn}$ alloy, the stability of ORR is enhanced with the increase of manganese content, which may be related to the stability of crystal structure and the interaction force between atoms [21,47].

3.4. MEA tests in a fuel cell

Based on the high activity and durability of the $\text{L1}_0\text{-PtCo}_{0.8}\text{Mn}_{0.2}$ catalyst in ORR, we further explored its use as a MEA cathode in fuel cell testing under $\text{H}_2\text{-O}_2\text{/Air}$ conditions to evaluate its practical performance in PEMFCs. For comparison, we used commercial platinum carbon with

high specific surface area and $\text{L1}_0\text{-PtCo}$ as cathode catalysts to compare their performance under the same PEMFC operating conditions. As shown in Fig. 6a, the mass activity ($\text{MA}_{\text{iR-free}}$, corrected by high-frequency resistance) of the $\text{L1}_0\text{-PtCo}_{0.8}\text{Mn}_{0.2}$ catalyst is 0.954 A/mg_{Pt}, which is higher than the 0.47 A/mg_{Pt} of Pt/C, indicating its significantly improved kinetics. Additionally, the Tafel slope (Fig. 6d) of catalyst mass activity also shows that $\text{L1}_0\text{-PtCo}_{0.8}\text{Mn}_{0.2}$ has a higher improvement.

Figures S14(a and b) show the effect of the cathode noble metal loading on the intrinsic activity and mass transfer. The open circuit voltage and MA at 0.9 V of $\text{L1}_0\text{-PtCo}_{0.8}\text{Mn}_{0.2}$ catalyst for 0.1 mg_{Pt}cm⁻² metal loading can reach 0.989 V and 0.992 A/mg_{Pt}, respectively, significantly higher than Pt/C, which are close to the intrinsic values obtained in the half-cell tests, indicating that it has excellent intrinsic catalytic activity. Further comparing the relationship between the catalyst loading and the performance, we found that although we were slightly lower than the DOE's target (Cathode: ≤ 0.1 mg_{Pt}cm⁻², current density > 0.3 A/cm² at 0.8 V) at 0.1 mg_{Pt}cm⁻² noble metal loading, the power density at 0.8 V increased significantly when the noble metal

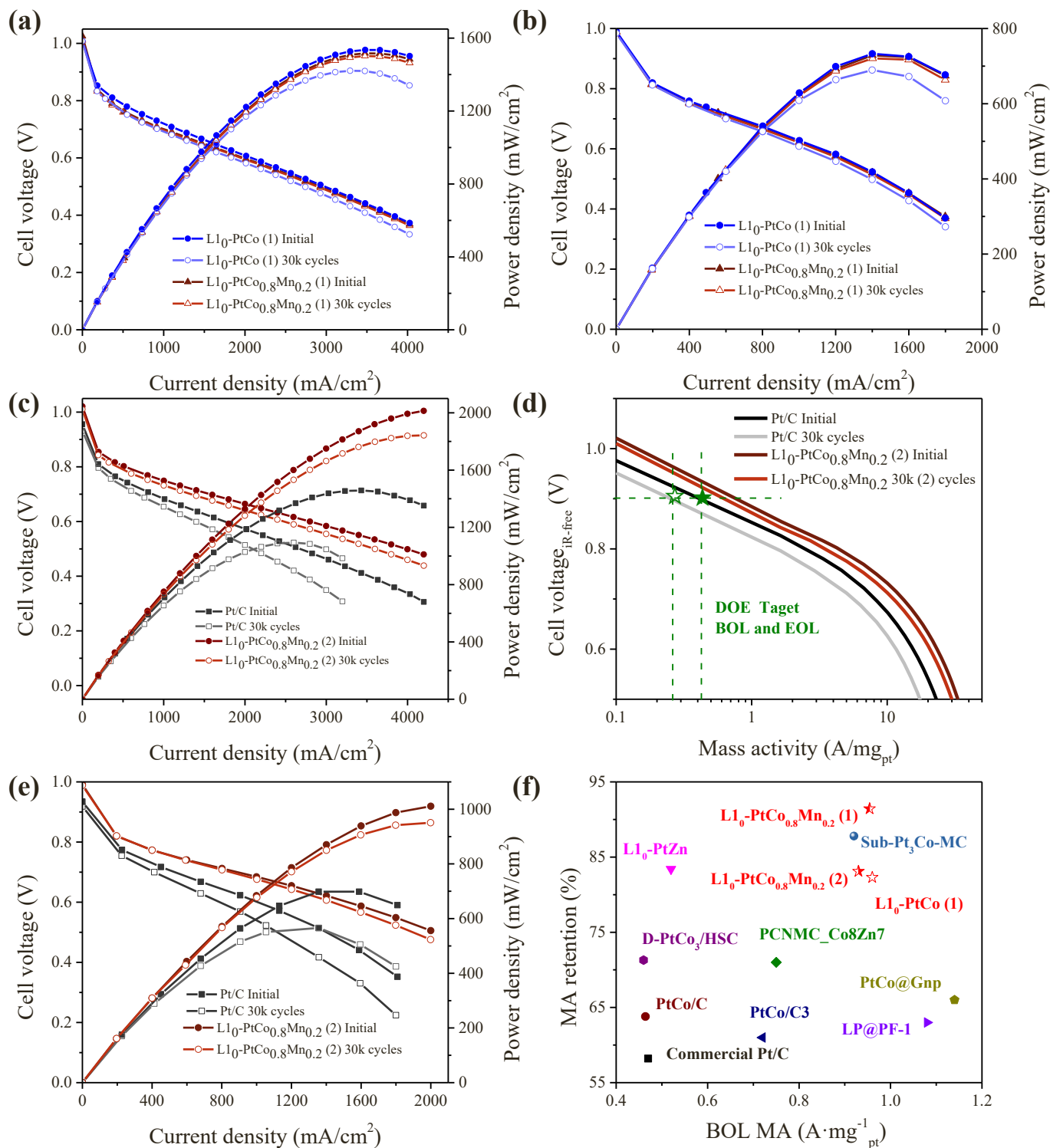


Fig. 6. Performance of the PEMFCs. (a) $\text{H}_2\text{-O}_2$ fuel cell polarization curves of L10-PtCo (1, 16.12 wt%), $\text{L10-PtCo}_{0.8}\text{Mn}_{0.2}$ (1, 15.96 wt%). Anode: $0.2 \text{ mg}_{\text{Pt}}/\text{cm}^2 \text{ Pt/C}$, Cathode: $0.12 \text{ mg}_{\text{Pt}}/\text{cm}^2 \text{ L10-PtCo}$ or $\text{L10-PtCo}_{0.8}\text{Mn}_{0.2}$. (b) $\text{H}_2\text{-Air}$ fuel cell polarization curves. (c) $\text{H}_2\text{-O}_2$ fuel cell polarization curves of $\text{L10-PtCo}_{0.8}\text{Mn}_{0.2}$ (2, 38.5 wt%) and Pt/C. Anode: $0.2 \text{ mg}_{\text{Pt}}/\text{cm}^2 \text{ Pt/C}$, Cathode: $0.12 \text{ mg}_{\text{Pt}}/\text{cm}^2 \text{ L10-PtCo}_{0.8}\text{Mn}_{0.2}$ or commercial Pt/C. (d) Tafel slope plot of MA. (e) $\text{H}_2\text{-Air}$ fuel cell polarization curves. (f) Comparison of BOL and EOL MA between $\text{L10-PtCo}_{0.8}\text{Mn}_{0.2}$ and the advanced catalysts in the literature, H_2/O_2 fuel cell.

loading increased to $0.12 \text{ mg}_{\text{Pt}}/\text{cm}^2$ [5,48]. Notably, with the increase of the cathode noble metal loading, the power density and the corresponding working current at 0.8 V continue to increase, and there is a high open circuit voltage of 1.032 V at $0.2 \text{ mg}_{\text{Pt}}/\text{cm}^2$, but when the catalyst loading exceeds $0.120 \text{ mg}_{\text{Pt}}/\text{cm}^2$, the MA of the catalyst decreases (Figure S14c). Therefore, the performance and cost of membrane

electrode should be comprehensively considered to meet the needs of the actual working conditions of fuel cells [49,50].

We used an updated square-wave cycle protocol to evaluate the stability of catalysts under $\text{H}_2\text{-O}_2/\text{Air}$ conditions. As shown in Figure 6(a & c), the $\text{L10-PtCo}_{0.8}\text{Mn}_{0.2}$ retained 91.4% of its initial MA after 30k cycles of ADT, which is hugely higher than Pt/C (58.2%) and L10-PtCo

(82.3%), for same loadings, and represents a very high durability compared to other reported work (Fig. 6f and Table S6) [20,33,48, 51–53]. At the same time, it has been demonstrated that L1₀-PtCo_{0.8}Mn_{0.2} exhibits better stability than L1₀-PtCo in fuel cell testing, which is consistent with the results of our half-cell testing. As shown in Figures S15(a & b), the L1₀-PtCo_{0.8}Mn_{0.2} (1) shows a voltage drop of ~ 5 mV after 30,000 cycles ADT, which is hugely lower than the loss of the DOE's target (At a current density of 0.8 A/cm², <30 mV). Meanwhile, as shown in Figure S15c, the power density at 0.65 V is decreased by only ~ 2.5%, from 0.968 W/cm² to 0.944 W/cm². In addition, as shown in Figure S17 and Figure S18, there are significant differences in the HAADF-STEM and EDS elemental mapping of L1₀-PtCo_{0.8}Mn_{0.2} and L1₀-PtCo after ADT 30000 cycles. There was no significant dissolution in the elemental mapping before (Fig. 3(e-h)) and after the stability test of the L1₀-PtCo_{0.8}Mn_{0.2} catalyst (Figure S17), showing good stability, while the Co element of L1₀-PtCo partially dissolved and the atoms decreased to Pt:Co=69:31(Table S7).

Although H₂/O₂ fuel cell testing can better demonstrate the intrinsic activity of oxygen reduction catalysts, testing in H₂/Air fuel cells can

better reflect actual working conditions. As shown in Fig. 6b, under the same catalyst loading, L1₀-PtCo_{0.8}Mn_{0.2} and L1₀-PtCo exhibit better catalytic activity than commercial Pt/C, with power densities of 0.728 and 0.732 W/cm² (Pt/C:0.699 W/cm²), respectively. Obviously, it still exhibits good durability under air testing conditions and exhibits the same conclusion as H₂/O₂ fuel cells, while the performance of H₂/Air fuel cells seems low. Therefore, we further tested catalysts with higher weight percentages to reduce the impact of mass transfer on performance. As shown in Fig. 6c and Figure S18, compared to the low weight percentage power density, the performance of fuel cells has been significantly improved, with a peak power density of 2.02 W/cm². It is worth mentioning that although the durability has decreased compared to low mass percentage, it still shows high durability, achieving a MA retention of 83.1% in H₂/O₂ fuel cells. Simultaneously, in Fig. 6e and Figure S15d, the power density of the catalyst has also been significantly improved, reaching 1.01 W/cm², indicating that optimizing the catalytic layer structure can effectively improve the performance of fuel cells.

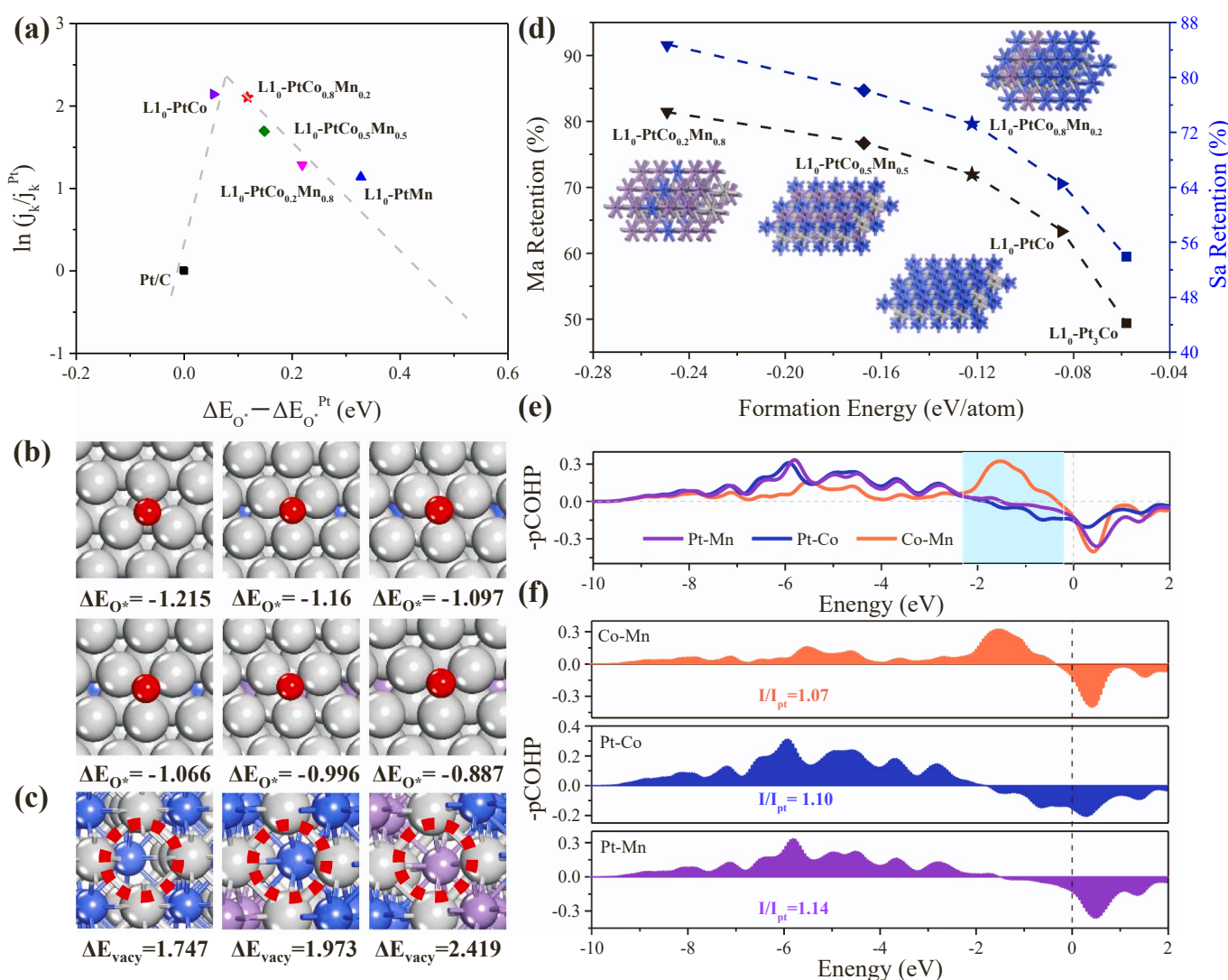


Fig. 7. Catalyst performance and durability mechanism for ORR by theoretical calculation. (a) The functional relationship between the kinetic current and the ΔE_{O^*} . The dashed lines are the theoretical predictions from our work and references. (b) Adsorption models and energies values of O^* intermediate on different catalysts (111) plane. First row: Pt(left), L1₀-PtCo (middle), L1₀-PtCo_{0.8}Mn_{0.2}(right); Second row: L1₀-PtCo_{0.5}Mn_{0.5}(left), L1₀-PtCo_{0.2}Mn_{0.8}(middle), L1₀-PtMn (right), respectively. (c) Structural models and their corresponding vacancy formation energy (ΔE_{vacy}) values. Red Circle: Co vacancy of L1₀-PtCo, Co vacancy of L1₀-PtCo_{0.8}Mn_{0.2}, Mn vacancy of L1₀-PtCo_{0.8}Mn_{0.2}, respectively. (d) The MA retention and SA retention of some alloy electrocatalysts reported in this work are functions of the calculated alloy formation energy. (e-f) Bonding analysis between different atoms in L1₀-PtCo_{0.8}Mn_{0.2} alloy using COHP and ICOHP.

3.5. DFT explores the mechanism of ORR activity and durability

The DFT calculations were conducted to investigate the enhancement mechanism in the ordered intermetallic L1₀-PtCoMn nanocatalysts in terms of ORR activity and durability. Fig. 7a shows the experimental activity data along with a dotted line that represents the predicted activity based on ΔE_{O^*} . Interestingly, by plotting the activity and adsorption energy function curves, we obtained a simple volcano diagram similar to the Sabatier [54,55] principle, indicating that this relationship also exists in the composition engineering of L1₀-PtCoMn NPs alloys. Although the relationship between adsorption energy and reaction activity shows that our predicted optimal adsorption value deviates from that of J. K. Nørskov and co-workers by ~ 0.1 eV, the predicted activity trend is accurate [42,56,57].

Experimental data and models clearly indicate that the weaker adsorption on Pt (111) surface of L1₀-PtCoMn leads to better ORR activity than Pt, and L1₀-PtCo_{0.8}Mn_{0.2} exhibits the optimal adsorption in the L1₀-PtCoMn ternary intermetallic nanocatalyst. The value of ΔE_{O^*} and the typical models of O^{*} adsorbed on hollow site of Pt (111) surface, as shown in Fig. 7b. In alloy systems of different components, the O^{*} intermediates can all combine at the same site to form an energetically favorable state. The ΔE_{O^*} of ordered intermetallic L1₀-PtCoMn nanoparticles increases with the increase of Co atoms in the composition, indicating that the ligand and strain effects of the alloy greatly affect the adsorption of the O^{*} intermediate at the Pt site [4,5,58–60]. Hence, we provide a powerful reference for exploring multicomponent alloy catalysts for ORR.

We have revealed the stability mechanism of catalyst from three aspects: catalyst structure stability, atomic vacancy diffusion barrier and interaction forces. To analyze the structural stability of L1₀-PtCoMn NPs alloys, the formation energy of each atom of a ternary alloy compound (ΔE_{vacy}) was calculated. By establishing the functional relationship between MA retention and SA retention of the ORR and the formation energy of the structure, it is shown that the more negative ΔE_{form} , the better the stability of the catalyst (Fig. 7d). Particularly, the increase in Mn components in L1₀-PtCoMn NPs alloys results in a more negative structural formation energy and better catalytic stability in ORR, indicating that Mn atoms play an essential role in the stability mechanism, which is related to atomic interaction forces of Mn in the alloy. Schiøtz et al. [21] found that the ΔE_{form} can be used as a descriptor for the durability of fuel cell catalysts, and that the vacancy diffusion potential barrier of a few elements in the alloy is related to ΔE_{form} . Therefore, as shown in Fig. 7c, we describe the vacancy diffusion potential barrier of alloy catalysts in fuel cells by calculating the vacancy formation energies of L1₀-PtCo_{0.8}Mn_{0.2} (Co and Mn vacancy) and L1₀-PtCo (Co vacancy), and then explore the stability of the catalysts. Compared to 1.747 eV of Co_{vacy} for L1₀-PtCo, the Co_{vacy} and Mn_{vacy} for L1₀-PtCo_{0.8}Mn_{0.2} are 1.973 and 2.419 eV, respectively, indicating that L1₀-PtCo_{0.8}Mn_{0.2} has better stability as cathode catalysts in ORR, consistent with the above formation energy and experimental results.

Furthermore, the COHP can project the off-domain electron density to analyze bonding interactions between metal atoms [61]. For convenience, we draw a functional relationship between -p COHP (“projected” COHP) and energy, that is, positive values are the contributions of bonding orbits and negative values are the contributions of antibonding molecular orbital. As shown in Fig. 7e, below the Fermi level, it can be clearly seen that most of them are bonded states, which is conducive to the formation of stable structures [11]. Especially for the Co-Mn bond, it has a large bonding region from -2 eV to 0 eV, eliminating the effect of Pt-Co and Pt-Mn antibonding states. As shown in Fig. 7f, we considered the Ip-COHP ratio of bond strength, and the interaction force between these three bonds is greater than that of Pt-Pt bonds, indicating that in L1₀-PtCo_{0.2}Mn_{0.8} alloy, both Co and Mn atoms have strong interactions. In addition, the ICOHP of Pt-Mn in L1₀-PtCo_{0.8}Mn_{0.2} alloy is bigger than that of Pt-Co, indicating that Pt-Mn has a slightly stronger interaction force. Therefore, through COHP calculations, it is shown that the

presence of Mn atoms in L1₀-PtCo_{0.8}Mn_{0.2} alloy enhances the bonding state and interatomic interaction forces, thereby improving the stability of the alloy.

4. Conclusions

In summary, we synthesized sub-6 nm L1₀-PtCoMn alloy with carbon coating and investigated the effect of alloy composition engineering on the ORR in PEMFCs. Compared to other components of alloys, the L1₀-PtCo_{0.8}Mn_{0.2} has the most efficient activity and stability in the half-cell. The L1₀-PtCo_{0.8}Mn_{0.2} catalyst exhibits high stability and high activity in fuel cells, with MA of 0.954 A/mg_{Pt} and only $\sim 8.6\%$ loss after 30k cycles, which exceeds the target set by DOE for activity and stability. Based on experimental data and DFT calculations, a volcanic diagram of adsorption energy (ΔE_{O^*}) and reaction activity was obtained, indicating that L1₀-PtCo_{0.8}Mn_{0.2} exhibits appropriate adsorption, thereby improving the performance of ORR. DFT calculations further confirmed that the excellent stability of L1₀-PtCo_{0.8}Mn_{0.2} lies in the fact that Mn increases the formation energy of the alloy, stabilizes the structure, and enhances bonding and atomic interactions in the alloy.

CRedit authorship contribution statement

Liu Xi-hao: Writing – original draft, Methodology. **Feng Huiyan:** Validation, Methodology. **Liu Jia:** Validation, Methodology, Formal analysis. **Chen Zhen-Yu:** Validation, Methodology. **Qin Shou-Guo:** Investigation, Formal analysis, Conceptualization. **Feng Yudan:** Writing – review & editing, Validation. **Tian Zhi-Qun:** Validation, Conceptualization. **Tsiakaras Panagiotis:** Writing – review & editing, Validation, Conceptualization. **Shen Pei-Kang:** Writing – review & editing, Resources, Funding acquisition, Conceptualization.

Declaration of Competing Interest

The authors declare that they have no known competing financial interests or personal relationships that could have appeared to influence the work reported in this paper.

Data Availability

Data will be made available on request.

Acknowledgements

The work was supported by Key Project of the Regional Innovation and Development Joint Fund of the National Natural Science Foundation of China, Project No. U22A20253.

Appendix A. Supporting information

Supplementary data associated with this article can be found in the online version at doi:10.1016/j.apcatb.2024.123832.

References

- [1] S. Zaman, L. Huang, A.I. Douka, H. Yang, B. You, B.Y. Xia, Oxygen Reduction Electrocatalysts toward Practical Fuel Cells: Progress and Perspectives, *Angew. Chem. Int. Ed. Engl.* 60 (2021) 17832–17852, <https://doi.org/10.1002/anie.202016977>.
- [2] Z. Liu, Z. Zhao, B. Peng, X. Duan, Y. Huang, Beyond extended surfaces: understanding the oxygen reduction reaction on nanocatalysts, *J. Am. Chem. Soc.* 142 (2020) 17812–17827, <https://doi.org/10.1021/jacs.0c07696>.
- [3] A. Kulkarni, S. Siahrostami, A. Patel, J.K. Nørskov, Understanding catalytic activity trends in the oxygen reduction reaction, *Chem. Rev.* 118 (2018) 2302–2312, <https://doi.org/10.1021/acs.chemrev.7b00488>.
- [4] J.R. Li, S. Sharma, X.M. Liu, Y.T. Pan, J.S. Spendelow, M.F. Chi, Y.K. Jia, P. Zhang, D.A. Cullen, Z. Xi, H.H. Lin, Z.Y. Yin, B. Shen, M. Muzzio, C. Yu, Y.S. Kim, A. A. Peterson, K.L. More, H.Y. Zhu, S.H. Sun, Hard-magnet L1(0)-CoPt nanoparticles

advance fuel cell catalysis, Joule 3 (2019) 124–135, <https://doi.org/10.1016/j.joule.2018.09.016>.

[5] Q. Cheng, S. Yang, C. Fu, L. Zou, Z. Zou, Z. Jiang, J. Zhang, H. Yang, High-loaded sub-6 nm Pt1Co1 intermetallic compounds with highly efficient performance expression in PEMFCs, Energy Environ. Sci. 15 (2022) 278–286, <https://doi.org/10.1039/dle02530a>.

[6] D.Y. Chung, S.W. Jun, G. Yoon, S.G. Kwon, D.Y. Shin, P. Seo, J.M. Yoo, H. Shin, Y. H. Chung, H. Kim, B.S. Mun, K.S. Lee, N.S. Lee, S.J. Yoo, D.H. Lim, K. Kang, Y. E. Sung, T. Hyeon, Highly Durable and active PtFe nanocatalyst for electrochemical oxygen reduction reaction, J. Am. Chem. Soc. 137 (2015) 15478–15485, <https://doi.org/10.1021/jacs.5b09653>.

[7] Z.Y. Qi, Y.C. Pei, T.W. Goh, Z.Y. Wang, X.L. Li, M. Lowe, R.V. Maligal-Ganesh, W. Y. Huang, Conversion of confined metal@ZIF-8 structures to intermetallic nanoparticles supported on nitrogen-doped carbon for electrocatalysis, Nano Res. 11 (2018) 3469–3479, <https://doi.org/10.1007/s12274-018-2016-x>.

[8] T. Lazaridis, B.M. Stuhmeier, H.A. Gasteiger, H.A. El-Sayed, Capabilities and limitations of rotating disk electrodes versus membrane electrode assemblies in the investigation of electrocatalysts, Nat. Catal. 5 (2022) 363–373, <https://doi.org/10.1038/s41929-022-00776-5>.

[9] J.C. Meier, I. Katsounaros, C. Galeano, H.J. Bongard, A.A. Topalov, A. Kostka, A. Karschin, F. Schut, K.J.J. Mayrhofer, Stability investigations of electrocatalysts on the nanoscale, Energy Environ. Sci. 5 (2012) 9319–9330, <https://doi.org/10.1039/c2ee22550f>.

[10] X. Zhu, L. Huang, M. Wei, P. Tsiaikaras, P.K. Shen, Highly stable Pt-Co nanodendrite in nanoframe with Pt skin structured catalyst for oxygen reduction electrocatalysis, Appl. Catal. B: Environ. 281 (2021), <https://doi.org/10.1016/j.apcatb.2020.119460>.

[11] W. Tu, W. Luo, C. Chen, K. Chen, E. Zhu, Z. Zhao, Z. Wang, T. Hu, H. Zai, X. Ke, M. Sui, P. Chen, Q. Zhang, Q. Chen, Y. Li, Y. Huang, Tungsten as “adhesive” in Pt2CuW0.25 ternary alloy for highly durable oxygen reduction electrocatalysis, Adv. Funct. Mater. 30 (2019) 1908230, <https://doi.org/10.1002/adfm.201908230>.

[12] X. Liu, Z. Zhao, J. Liang, S. Li, G. Lu, C. Priest, T. Wang, J. Han, G. Wu, X. Wang, Y. Huang, Q. Li, Inducing covalent atomic interaction in intermetallic Pt alloy nanocatalysts for high-performance fuel cells, Angew. Chem. Int. Ed. Engl. (2023) e202302134, <https://doi.org/10.1002/anie.202302134>.

[13] W. Zhao, B. Chi, L. Liang, P. Yang, W. Zhang, X. Ge, L. Wang, Z. Cui, S. Liao, Optimizing the electronic structure of ordered Pt–Co–Ti ternary intermetallic catalyst to boost acidic oxygen reduction, ACS Catal. 12 (2022) 7571–7578, <https://doi.org/10.1021/acscatal.2c00554>.

[14] M. Zhou, C. Li, J. Fang, Noble-metal based random alloy and intermetallic nanocrystals: syntheses and applications, Chem. Rev. 121 (2021) 736–795, <https://doi.org/10.1021/acs.chemrev.0c00436>.

[15] U. Mizutani, Hume-Rothery rules for structurally complex alloy phases, MRS Bull. 37 (2012) 169–1612, <https://doi.org/10.1557/mrs.2012.45>.

[16] C.L. Yang, L.N. Wang, P. Yin, J. Liu, M.X. Chen, Q.Q. Yan, Z.S. Wang, S.L. Xu, S. Q. Chu, C. Cui, H. Ju, J. Zhu, Y. Lin, J. Shui, H.W. Liang, Sulfur-anchoring synthesis of platinum intermetallic nanoparticle catalysts for fuel cells, Science 374 (2021) 459–464, <https://doi.org/10.1126/science.abj9980>.

[17] J.S. Liang, F. Ma, S. Hwang, X.X. Wang, J. Sokolowski, Q. Li, G. Wu, D. Su, Atomic Arrangement engineering of metallic nanocrystals for energy-conversion electrocatalysis, Joule 3 (2019) 956–991, <https://doi.org/10.1016/j.joule.2019.03.014>.

[18] P.F. Ladwig, Y.A. Chang, E.S. Linville, A. Morrone, J. Gao, B.B. Pant, A.E. Schlutz, S. Mao, Paramagnetic to antiferromagnetic phase transformation in sputter deposited Pt–Mn thin films, J. Appl. Phys. 94 (2003) 979–987, <https://doi.org/10.1063/1.1587266>.

[19] R.A. Ristau, K. Barmak, L.H. Lewis, K.R. Coffey, J.K. Howard, On the relationship of high coercivity and L1(0) ordered phase in CoPt and FePt thin films, J. Appl. Phys. 86 (1999) 4527–4533, <https://doi.org/10.1063/1.371397>.

[20] J.S. Liang, Z.L. Zhao, N. Li, X.M. Wang, S.Z. Li, X. Liu, T.Y. Wang, G. Lu, D.L. Wang, B.J. Hwang, Y.H. Huang, D. Su, Q. Li, Biaxial strains mediated oxygen reduction electrocatalysis on fenton reaction resistant L1(0)-PtZn fuel cell cathode, Adv. Energy Mater. 10 (2020), <https://doi.org/10.1002/aenm.202000179>.

[21] U.G. Vej-Hansen, J. Rossmeisl, I.E. Stephens, J. Schiottz, Correlation between diffusion barriers and alloying energy in binary alloys, Phys. Chem. Chem. Phys. 18 (2016) 3302–3307, <https://doi.org/10.1039/c5cp04694g>.

[22] M. Karuppannan, Y. Kim, S. Gok, E. Lee, J.Y. Hwang, J.-H. Jang, Y.-H. Cho, T. Lim, Y.-E. Sung, O.J. Kwon, A highly durable carbon-nanofiber-supported Pt–C core–shell cathode catalyst for ultra-low Pt loading proton exchange membrane fuel cells: facile carbon encapsulation, Energy Environ. Sci. 12 (2019) 2820–2829, <https://doi.org/10.1039/c9ee01000a>.

[23] S.Q. He, Y. Liu, H.B. Zhan, L.H. Guan, Direct thermal annealing synthesis of ordered Pt alloy nanoparticles coated with a thin N-doped carbon shell for the oxygen reduction reaction, ACS Catal. 11 (2021) 9355–9365, <https://doi.org/10.1021/acscatal.1c02434>.

[24] G. Kresse, J. Furthmuller, Efficiency of ab-initio total energy calculations for metals and semiconductors using a plane-wave basis set, Comput. Mater. Sci. 6 (1996) 15–50, [https://doi.org/10.1016/0927-0256\(96\)00008-0](https://doi.org/10.1016/0927-0256(96)00008-0).

[25] P.E. Blochl, Projector augmented-wave method, Phys. Rev. B Condens Matter 50 (1994) 17953–17979, <https://doi.org/10.1103/physrevb.50.17953>.

[26] J.P. Perdew, J.A. Chevary, S.H. Vosko, K.A. Jackson, M.R. Pederson, D.J. Singh, C. Fiolhais, Atoms, molecules, solids, and surfaces: Applications of the generalized gradient approximation for exchange and correlation, Phys. Rev. B Condens Matter 46 (1992) 6671–6687, <https://doi.org/10.1103/physrevb.46.6671>.

[27] B.R. Sahu, Electronic structure and bonding of ultralight LiMg, Mater. Sci. Eng.: B 49 (1997) 74–78, [https://doi.org/10.1016/s0921-5107\(97\)00068-8](https://doi.org/10.1016/s0921-5107(97)00068-8).

[28] V.L. Deringer, A.L. Tchougreeff, R. Dronskowski, Crystal orbital Hamilton population (COHP) analysis as projected from plane-wave basis sets, J. Phys. Chem. A 115 (2011) 5461–5466, <https://doi.org/10.1021/jp202489s>.

[29] M. Chi, C. Wang, Y. Lei, G. Wang, D. Li, K.L. More, A. Lupini, L.F. Allard, N. M. Markovic, V.R. Stamenkovic, Surface faceting and elemental diffusion behaviour at atomic scale for alloy nanoparticles during *in situ* annealing, Nat. Commun. 6 (2015) 8925, <https://doi.org/10.1038/ncomms9925>.

[30] Z.J. Zhao, S.H. Liu, S.J. Zha, D.F. Cheng, F. Studt, G. Henkelman, J.L. Gong, Theory-guided design of catalytic materials using scaling relationships and reactivity descriptors, Nat. Rev. Mater. 4 (2019) 792–804, <https://doi.org/10.1038/s41578-019-0152-x>.

[31] H. Kuroki, T. Tamaki, M. Matsumoto, M. Arao, K. Kubobuchi, H. Imai, T. Yamaguchi, Platinum–iron–nickel trimetallic catalyst with superlattice structure for enhanced oxygen reduction activity and durability, Ind. Eng. Chem. Res. 55 (2016) 11458–11466, <https://doi.org/10.1021/acs.iecr.6b02298>.

[32] T. Wang, J. Liang, Z. Zhao, S. Li, G. Lu, Z. Xia, C. Wang, J. Luo, J. Han, C. Ma, Y. Huang, Q. Li, Sub-6 nm fully ordered Li₁-Pt–Ni–Co nanoparticles enhance oxygen reduction via Co doping induced ferromagnetism enhancement and optimized surface strain, Adv. Energy Mater. 9 (2019), <https://doi.org/10.1002/aenm.201803771>.

[33] L. Chong, J. Wen, J. Kubal, F.G. Sen, J. Zou, J. Greeley, M. Chan, H. Barkholtz, W. Ding, D.J. Liu, Ultralow-loading platinum–cobalt fuel cell catalysts derived from imidazolate frameworks, Science 362 (2018) 1276–1281, <https://doi.org/10.1126/science.aau0630>.

[34] G.W. Sievers, A.W. Jensen, J. Quinson, A. Zana, F. Bizzotto, M. Oezaslan, A. Dworzak, J.J.K. Kirkensgaard, T.E.L. Smitshuisen, S. Kadkhodazadeh, M. Juelsholt, K.M.O. Jensen, K. Anklam, H. Wan, J. Schafer, K. Cepe, M. Escudero-Escobar, J. Rossmeisl, A. Quade, V. Bruser, M. Arenz, Self-supported Pt–Co networks combining high specific activity with high surface area for oxygen reduction, Nat. Mater. 20 (2021) 208–213, <https://doi.org/10.1038/s41563-020-0775-8>.

[35] P. Strasser, S. Koh, T. Anniyev, J. Greeley, K. More, C. Yu, Z. Liu, S. Kaya, D. Nordlund, H. Ogasawara, M.F. Toney, A. Nilsson, Lattice-strain control of the activity in dealloyed core–shell fuel cell catalysts, Nat. Chem. 2 (2010) 454–460, <https://doi.org/10.1038/nchem.623>.

[36] Q. Li, L. Wu, G. Wu, D. Su, H. Lv, S. Zhang, W. Zhu, A. Casimir, H. Zhu, A. Mendoza-Garcia, S. Sun, New approach to fully ordered fct–FePt nanoparticles for much enhanced electrocatalysis in acid, Nano Lett. 15 (2015) 2468–2473, <https://doi.org/10.1021/acs.nanolett.5b00320>.

[37] R. Yadav, C.H. Wu, I.F. Huang, X. Li, T.H. Wu, K.W. Lin, Effects of perpendicular magnetic field annealing on the structural and magnetic properties of [Co/Ni](2)/PtMn thin films, Magnetochemistry 7 (2021), <https://doi.org/10.3390/magnetochemistry7030038>.

[38] Y. Yu, W. Yang, X. Sun, W. Zhu, X.Z. Li, D.J. Sellmyer, S. Sun, Monodisperse MPT (M = Fe, Co, Ni, Cu, Zn) nanoparticles prepared from a facile oleylamine reduction of metal salts, Nano Lett. 14 (2014) 2778–2782, <https://doi.org/10.1021/nl500776e>.

[39] T.Y. Yoo, J.M. Yoo, A.K. Sinha, M.S. Bootharaju, E. Jung, H.S. Lee, B.H. Lee, J. Kim, W.H. Antink, Y.M. Kim, J. Lee, E. Lee, D.W. Lee, S.P. Cho, S.J. Yoo, Y.E. Sung, T. Hyeon, Direct Synthesis of intermetallic platinum–alloy nanoparticles highly loaded on carbon supports for efficient electrocatalysis, J. Am. Chem. Soc. 142 (2020) 14190–14200, <https://doi.org/10.1021/jacs.0c05140>.

[40] J. Li, Z. Xi, Y.T. Pan, J.S. Spendelow, P.N. Duchesne, D. Su, Q. Li, C. Yu, Z. Yin, B. Shen, Y.S. Kim, P. Zhang, S. Sun, Fe Stabilization by intermetallic L1(0)-FePt and Pt catalysis enhancement in L1(0)-FePt/Pt nanoparticles for efficient oxygen reduction reaction in fuel cells, J. Am. Chem. Soc. 140 (2018) 2926–2932, <https://doi.org/10.1021/ja812829>.

[41] B.A. Lu, L.F. Shen, J. Liu, Q.H. Zhang, L.Y. Wan, D.J. Morris, R.X. Wang, Z.Y. Zhou, G. Li, T. Sheng, L. Gu, P. Zhang, N. Tian, S.G. Sun, Structurally disordered phosphorus-doped Pt as a highly active electrocatalyst for an oxygen reduction reaction, Acs Catal. 11 (2021) 355–363, <https://doi.org/10.1021/acscatal.0c03137>.

[42] V. Stamenkovic, B.S. Mun, K.J. Mayrhofer, P.N. Ross, N.M. Markovic, J. Rossmeisl, J. Greeley, J.K. Norskov, Changing the activity of electrocatalysts for oxygen reduction by tuning the surface electronic structure, Angew. Chem. Int. Ed. Engl. 45 (2006) 2897–2901, <https://doi.org/10.1002/anie.200504386>.

[43] P. Zhao, X. Qin, H. Li, K. Qu, R. Li, New insights into O and OH adsorption on the Pt–Co alloy surface: effects of Pt/Co ratios and structures, Phys. Chem. Chem. Phys. 22 (2020) 21124–21130, <https://doi.org/10.1039/dcp02746d>.

[44] C. Xiao, B.A. Lu, P. Xue, N. Tian, Y.Z. Zhou, X. Lin, W.F. Lin, S.G. Sun, High-Index-Facet- and High-Surface-Energy Nanocrystals of Metals and Metal Oxides as Highly Efficient Catalysts, Joule 4 (2020) 2562–2598, <https://doi.org/10.1016/j.joule.2020.10.002>.

[45] S. Rudi, C. Cui, L. Gan, P. Strasser, Comparative study of the electrocatalytically active surface areas (ECSAs) of Pt alloy nanoparticles evaluated by Hupd and CO-stripping voltammetry, Electrocataylsis 5 (2014) 408–418, <https://doi.org/10.1007/s12678-014-0205-2>.

[46] M. Lukaszewski, Electrochemical methods of real surface area determination of noble metal electrodes – an overview, Int. J. Electrochem. Sci. (2016) 4442–4469, <https://doi.org/10.20964/2016.06.71>.

[47] T. Patniboon, H.A. Hansen, Acid-stable and active M–N–C catalysts for the oxygen reduction reaction: the role of local structure, ACS Catal. 11 (2021) 13102–13118, <https://doi.org/10.1021/acscatal.1c02941>.

[48] Z. Zhao, Z. Liu, A. Zhang, X. Yan, W. Xue, B. Peng, H.L. Xin, X. Pan, X. Duan, Y. Huang, Graphene-nanopocket-engaged PtCo nanocatalysts for highly durable fuel cell operation under demanding ultralow-Pt-loading conditions, *Nat. Nanotechnol.* 17 (2022) 968–975, <https://doi.org/10.1038/s41565-022-01170-9>.

[49] J.T. Fan, M. Chen, Z.L. Zhao, Z. Zhang, S.Y. Ye, S.Y. Xu, H.J. Wang, H. Li, Bridging the gap between highly active oxygen reduction reaction catalysts and effective catalyst layers for proton exchange membrane fuel cells, *Nat. Energy* 6 (2021) 475–486, <https://doi.org/10.1038/s41560-021-00824-7>.

[50] K. Jiao, J. Xuan, Q. Du, Z. Bao, B. Xie, B. Wang, Y. Zhao, L. Fan, H. Wang, Z. Hou, S. Huo, N.P. Brandon, Y. Yin, M.D. Guiver, Designing the next generation of proton-exchange membrane fuel cells, *Nature* 595 (2021) 361–369, <https://doi.org/10.1038/s41586-021-03482-7>.

[51] Z.P. Zhao, M.D. Hossain, C.C. Xu, Z.J. Lu, Y.S. Liu, S.H. Hsieh, I. Lee, W.P. Gao, J. Yang, B.V. Merinov, W. Xue, Z.Y. Liu, J.X. Zhou, Z.T. Luo, X.Q. Pan, F. Zaera, J. H. Guo, X.F. Duan, W.A. Goddard, Y. Huang, Tailoring a three-phase microenvironment for high-performance oxygen reduction reaction in proton exchange membrane fuel cells, *Matter* 3 (2020) 1774–1790, <https://doi.org/10.1016/j.matt.2020.09.025>.

[52] J.J. Slack, C. Gumeaci, N. Dale, J. Parrondo, N. Macauley, R. Mukundan, D. Cullen, B. Sneed, K. More, P.N. Pintauro, Nanofiber fuel cell MEAs with a PtCo/C cathode, *J. Electrochem. Soc.* 166 (2019) F3202–F3209, <https://doi.org/10.1149/2.0151907jes>.

[53] H. Cheng, R. Gui, H. Yu, C. Wang, S. Liu, H. Liu, T. Zhou, N. Zhang, X. Zheng, W. Chu, Y. Lin, H. Wu, C. Wu, Y. Xie, Subsize Pt-based intermetallic compound enables long-term cyclic mass activity for fuel-cell oxygen reduction, *Proc. Natl. Acad. Sci. USA* 118 (2021) e2104026118, <https://doi.org/10.1073/pnas.2104026118>.

[54] A. Logadottir, T.H. Rod, J.K. Nørskov, B. Hammer, S. Dahl, C.J.H. Jacobsen, The Brønsted–Evans–Polanyi relation and the volcano plot for ammonia synthesis over transition metal catalysts, *J. Catal.* 197 (2001) 229–231, <https://doi.org/10.1006/jcat.2000.3087>.

[55] J.K. Nørskov, J. Rossmeisl, A. Logadottir, L. Lindqvist, J.R. Kitchin, T. Bligaard, H. Jónsson, Origin of the overpotential for oxygen reduction at a fuel-cell cathode, *J. Phys. Chem. B* 108 (2004) 17886–17892, <https://doi.org/10.1021/jp047349j>.

[56] J. Greeley, I.E. Stephens, A.S. Bondarenko, T.P. Johansson, H.A. Hansen, T. F. Jaramillo, J. Rossmeisl, I. Chorkendorff, J.K. Nørskov, Alloys of platinum and early transition metals as oxygen reduction electrocatalysts, *Nat. Chem.* 1 (2009) 552–556, <https://doi.org/10.1038/nchem.367>.

[57] J. Zhang, M.B. Vukmirovic, Y. Xu, M. Mavrikakis, R.R. Adzic, Controlling the catalytic activity of platinum-monolayer electrocatalysts for oxygen reduction with different substrates, *Angew. Chem. Int. Ed. Engl.* 44 (2005) 2132–2135, <https://doi.org/10.1002/anie.200462335>.

[58] Q. Jia, K. Caldwell, K. Strickland, J.M. Ziegelbauer, Z. Liu, Z. Yu, D.E. Ramaker, S. Mukerjee, Improved oxygen reduction activity and durability of dealloyed PtCo (x) catalysts for proton exchange membrane fuel cells: strain, ligand, and particle size effects, *ACS Catal.* 5 (2015) 176–186, <https://doi.org/10.1021/cs501537n>.

[59] J. Li, S. Sharma, K. Wei, Z. Chen, D. Morris, H. Lin, C. Zeng, M. Chi, Z. Yin, M. Muzzio, M. Shen, P. Zhang, A.A. Peterson, S. Sun, Anisotropic strain tuning of Li(O) ternary nanoparticles for oxygen reduction, *J. Am. Chem. Soc.* 142 (2020) 19209–19216, <https://doi.org/10.1021/jacs.0c08962>.

[60] J.R. Kitchin, J.K. Nørskov, M.A. Barreau, J.G. Chen, Role of strain and ligand effects in the modification of the electronic and chemical properties of bimetallic surfaces, *Phys. Rev. Lett.* 93 (2004) 156801, <https://doi.org/10.1103/PhysRevLett.93.156801>.

[61] R. Dronskowski, P.E. Blöchl, Crystal orbital Hamilton populations (COHP): energy-resolved visualization of chemical bonding in solids based on density-functional calculations, *J. Phys. Chem.* 97 (2002) 8617–8624, <https://doi.org/10.1021/j100135a014>.